

Temperature properties in magnetised and radiatively cooled two-temperature accretion flows onto a black hole

Indu K. Dihingia,^{1,2,3}★ Yosuke Mizuno,^{2,4,5}† Christian M. Fromm,^{6,5,7} and Luciano Rezzolla^{5,8,9}

¹Department of Astronomy, Astrophysics and Space Engineering, Indian Institute of Technology Indore, Khandwa Road, Simrol 453552, India

²Tsung-Dao Lee Institute, Shanghai Jiao-Tong University, 520 Shengrong Road, Shanghai, 201210 People's Republic of China

³Department of Physics, Indian Institute of Science, Bangalore 560012, Karnataka, India

⁴School of Physics & Astronomy, Shanghai Jiao-Tong University, 800 Dongchuan Road, Shanghai, 200240, People's Republic of China

⁵Institut für Theoretische Physik, Goethe Universität, Max-von-Laue-Str. 1, 60438 Frankfurt am Main, Germany

⁶Institut für Theoretische Physik und Astrophysik, Julius Maximilian University, Würzburg, Emil-Fischer-Str. 31, D-97074 Würzburg, Germany

⁷Max-Planck-Institut für Radioastronomie, Auf dem Hügel 69, D-53121 Bonn, Germany

⁸School of Mathematics, Trinity College, Dublin 2, Ireland

⁹Frankfurt Institute for Advanced Studies, Ruth-Moufang-Str. 1, 60438 Frankfurt am Main, Germany

Accepted XXX. Received YYY; in original form ZZZ

ABSTRACT

Simplified assumptions about the thermodynamics of the electrons are normally employed in general-relativistic magnetohydrodynamic (GRMHD) simulations of accretion onto black holes. To counter this, we have developed a self-consistent approach to study magnetised and radiatively cooled two-temperature accretion flows around a Kerr black hole in two spatial dimensions. The approach includes several heating processes, radiative cooling, and a coupling between the electrons and the ions via Coulomb interaction. We test our approach by performing axisymmetric GRMHD simulations of magnetised tori accreting onto a Kerr black hole under various astrophysical scenarios. In this way, we find that the inclusion of the Coulomb interaction and the radiative cooling impacts the thermodynamical properties of both the ions and electrons, changing significantly the temperature distribution of the latter, and underlining the importance of a two-temperature approach when imaging these flows. In addition, we find that the accretion rate influences the bulk properties of the flow as well as the thermodynamics of the electrons and ions. Interestingly, we observe qualitatively distinct temperature properties for SANE and MAD accretion modes while maintaining the same accretion rates, which could help distinguishing MAD and SANE accretion flows via observations. Finally, we propose two new relations for the temperature ratios of the electrons, ions, and of the gas in terms of the plasma- β parameter. The new relations represent a simple and effective approach to treat two-temperature accretion flows on supermassive black holes such as Sgr A* and M 87*.

Key words: black hole physics – accretion, accretion discs – MHD – methods: numerical.

1 INTRODUCTION

Already in 1976, Shapiro et al. (1976) (hereafter SLE) proposed two-temperature accretion flows as a way to explain the observed spectra from Cyg X-1, where electrons and ions are regarded as two separate fluids with different temperatures. The SLE model has the benefit of a “hotter” solution for the accretion flow than the conventional Shakura & Sunyaev (1973) thin-disc model, which is plausible to explain observed hard X-rays in Cyg X-1. Soon after, the SLE model was used to investigate the spectral characteristics of X-Ray Binaries (XRBs) and Active Galactic Nuclei (AGNs) (e.g., Ichimaru (1977); Rees et al. (1982); Kusunose & Takahara (1988, 1989); White & Lightman (1989); Wandel & Liang (1991); Luo & Liang (1994). In addition, the SLE model was modified to include advection terms which remove the inherently thermally unstable nature of the model (Pringle 1976; Piran 1978), and it is explored in a wide range of

physical settings using a semi-analytic technique (Abramowicz et al. 1988; Kato et al. 1988; Narayan & Yi 1995; Esin et al. 1996; Nakamura et al. 1996; Manmoto et al. 1997; Rajesh & Mukhopadhyay 2010; Dihingia et al. 2018, 2020; Sarkar et al. 2020, etc.). While these semi-analytical models are crucial because they give a foundation for understanding the accretion processes around black holes in greater detail. However, numerical simulations are necessary to depict the realistic time-dependent, turbulent nature of the accretion flow.

General-relativistic magnetohydrodynamic (GRMHD) simulations are typically performed in a single-fluid or single-temperature approximation to comprehend emission near the black hole (e.g., Noble et al. 2007; Mościbrodzka et al. 2009, 2012, 2014, 2016; Dexter et al. 2009, 2010; Shcherbakov et al. 2012; Chan et al. 2015; Gold et al. 2017; Porth et al. 2017; Mizuno et al. 2018; Davelaar et al. 2018, 2019). The single-fluid approximation does not treat the temperatures of the electrons and ions self-consistently. As a result, the electron temperature required to calculate the electromagnetic emission needs to be estimated in some way from the gas temperature,

★ E-mail: idihingia@iiti.ac.in

† E-mail: mizuno@sjtu.edu.cn

which is computed self-consistently in the GRMHD simulations. Obviously, this estimate requires some suitable assumption from which to derive a prescription between the temperature of the electrons T_e and that of the ion/gas $T_{i/g}$.

These prescriptions are either very simple, e.g., a constant rescaling of the gas temperature (Mościbrodzka et al. 2009, 2014; Chan et al. 2015) or employ parametric models making use of the plasma- β distribution (Mościbrodzka et al. 2016; Anantua et al. 2020). One of the most commonly employed prescriptions for the electron temperature is the so-called $R - \beta$ prescription (Mościbrodzka et al. 2016), where the electron temperature is estimated from plasma- β with two parameters ($R_{\text{low}}, R_{\text{high}}, \beta_{\text{crit}}$). This prescription was utilised to develop synthetic emission maps to model the EHT observations of M 87* and Sgr A* (Event Horizon Telescope Collaboration et al. 2019, 2021, 2022). Often, a large number of these parameters ($R_{\text{low}}, R_{\text{high}}$) need to be tested to find a suitable combination/range of parameters that match the observations (e.g., Mizuno et al. 2021; Fromm et al. 2022; Cruz-Orsio et al. 2022). However, since the correlations of these parameters with the physics involved in the accretion flow are not known, it is difficult to translate the knowledge of the optimal parameters into the knowledge of the physical nature of the flow. Therefore, a physically motivated self-consistent two-temperature framework is important in order to obtain firm information from the observations, and this is one of the primary goals of this study.

Ressler et al. (2015) have performed two-temperature GRMHD simulations to incorporate electron thermodynamics self-consistently and applied them to understand the images and spectra of Sgr A* (Ressler et al. 2017). Their models produce sufficiently hot electrons that match the observed luminosity in NIR (near-infrared) bend. However, in their formalism, they only considered the effects of electron heating but neglected the radiative cooling and Coulomb interaction. Recently, Dexter et al. (2020a) performed an extensive parameter survey of two-temperature GRMHD simulations of magnetised accretion flows considering black-hole spins and different electron-heating prescriptions for Sgr A*. The study has explained the recently observed mean Faraday rotation and the polarised signals of NIR flares in Sgr A*. With the same numerical approach, Yao et al. (2021) reported comparable luminosity of very high-energy flares from M 87. However, they could not able to explain the timing properties of very high-energy flares in M 87. Subsequently, Sądowski et al. (2017) using an M1 approximation for the radiative transport, and Ryan et al. (2017) using a Monte Carlo scheme extended the formalism to incorporate effects from radiative feedback. Improved versions of this formalism has been recently applied to examine the images and timing properties of Sgr A* as well as M 87* (Chael et al. 2018; Ryan et al. 2018; Chael et al. 2019). Similar formalism is also applied to black hole X-ray binaries by Dexter et al. (2021), they studied accretion flows with different accretion rates around a stellar-mass black hole and found the collapse of hot accretion flows due to the thermal runaway.

Also, it is worth mentioning that single-fluid GRMHD with radiative cooling also has been explored to study hot accretion flow for Sgr A* (e.g., Fragile & Meier 2009; Dibi et al. 2012; Drappeau et al. 2013; Yoon et al. 2020). According to Yoon et al. (2020), the role of radiative cooling processes in the dynamics of the accretion flows increases with the accretion rate. They also identified a critical accretion rate that is $\dot{M} \gtrsim 10^{-7}$ times the Eddington limit; beyond this value, radiative cooling becomes dynamically important. However, in these works, the radiation-cooling rate is calculated from an adjusted electron temperature that assumes the ratio of electron to ion/gas temperature to be constant ($T_e/T_i = \text{constant}$). Such consideration

is not realistic and may introduce artificial effects in the underlying conclusions from these studies.

The goal of this study is to offer a formalism to obtain information on electron thermodynamics using a self-consistent two-temperature paradigm. To test this formalism, we perform axisymmetric 2D GRMHD simulations around a Kerr black hole. In this way, we investigate the transfer of energy from the ions to the electrons via the Coulomb-interaction process, which serves as a heating mechanism for the electrons and as a cooling mechanism for the ions. Additionally, electrons also gain energy through the turbulent heating process (Howes 2011). Finally, electrons can lose energy by several radiative mechanisms, such as Bremsstrahlung, synchrotron radiation, and the inverse Compton process. We illustrate the temperature distributions (T_e, T_i) in several physical scenarios and show the correlation of different temperatures and plasma- β from the simulation models. Future research will examine how these findings impact emission, spectra, and images computed with general-relativistic ray-tracing (GRRT) calculations.

The rest of the paper is organised as follows: Section 2 focuses on numerical and mathematical formalism, while Sec. 3 discusses the outcomes of our simulation models. Finally, Sec. 4 summarises and discusses our findings, as well as our future plans. Note that the Roman indices run from 1 to 3, while the Greek indices run from 0 to 3. Further, all the equations are solved in the code units, where G (gravitational constant) = M_\bullet (mass of the central black hole) = c (speed of light) = 1. Subsequently, we express the unit of mass, length, and time in terms of $M_\bullet, GM_\bullet/c^2$, and GM_\bullet/c^3 , respectively.

2 MATHEMATICAL AND PHYSICAL SETUP

For our simulations, we have employed the adaptive-mesh refinement (AMR) GRMHD code BHAC (Porth et al. 2017; Olivares et al. 2019) to perform 2D simulations of magnetised tori around a Kerr black hole. The ideal GRMHD equations can be expressed in terms of the conservation laws as follows (see Del Zanna et al. 2007; Rezzolla & Zanotti 2013),

$$\partial_t (\sqrt{\gamma}U) + \partial_i (\sqrt{\gamma}F^i) = \sqrt{\gamma}S. \quad (1)$$

In the presence of radiative cooling, we modify the source term as $S = S_0 + S'$, where S' is the additional contribution from radiation-cooling processes. The explicit expressions for the vectors of conserved variables U , fluxes F^i , and sources S_0 in the case of ideal GRMHD without radiative cooling have been reported by Porth et al. (2017) [see Eqs. (23) and (30) there]. The vector of conserved variables is given by $U \equiv [\mathcal{D}, \mathcal{S}_j, \tau, \mathcal{B}_j]^T$, where $\mathcal{D}, \mathcal{S}_j, \tau$, and \mathcal{B}_j refer to density, covariant three-momentum, the rescaled energy density, and magnetic three-fields in Eulerian frame, respectively (for detail follow Rezzolla & Zanotti 2013). On the other hand, the explicit form of the new source term S' can be expressed as follows

$$S' = \begin{pmatrix} 0 \\ -\alpha\gamma v_j \Lambda \\ -\alpha\gamma \Lambda \\ 0 \end{pmatrix}, \quad (2)$$

where α, γ, v_j , and Λ correspond to the lapse-function, Lorentz factor, fluid three-velocity, and the total radiation-cooling term, respectively. Note that here we consider the radiation-flux term to be proportional to the radiative cooling rate and the fluid velocity following Fragile & Meier (2009); Dibi et al. (2012); Yoon et al. (2020); both choices represent simplifications over a more accurate M1 moment

approach closure (e.g., Sądowski et al. 2017) or Montecarlo scheme (e.g., Ryan et al. 2017).

Equation (1) solves the single-fluid MHD equations containing electrons and ions. To extend our study to a two-temperature framework, we additionally solve the electron-entropy equation in the presence of dissipative heating, Coulomb interaction, and radiation-cooling processes, which is given by (see, e.g., Sądowski et al. 2017)

$$T_e \nabla_\mu (\rho u^\mu \kappa_e) = fQ + \Lambda_{ei} - \Lambda, \quad (3)$$

where $\kappa_e := \exp[(\tilde{\Gamma}_e - 1)s_e]$ and $s_e := p/\rho\tilde{\Gamma}_e$ is the electron entropy per particle. Here, $\tilde{\Gamma}_e$ is the adiabatic index of the electrons, Q is the rate of dissipative heating, and f is the fraction of dissipative heating transferred to the electrons. Λ_{ei} is the energy transferred to the electrons from the ions due to the Coulomb interaction. We also assume charge neutrality, i.e., $n = n_e = n_i$ (equal number densities for electrons and ions), and the four-velocities of the flow to be the same as the four-velocities of electrons and ions, i.e., $u^\mu = u_e^\mu = u_i^\mu$ when solving the electron-entropy equation. Here, we treat the dissipative-heating term following Ressler et al. (2015) and subsequently update the electron entropy explicitly following the conservation laws for electrons.

2.1 Dissipative and radiative processes

By solving Eqs. (1) and (3), we obtain all the properties of the flow and of the electrons. Using these properties, we estimate the internal energy density of the ions from the total internal energy density of the flow, and they are related as

$$u_{g,\text{int}} = u_{i,\text{int}} + u_{e,\text{int}}, \quad (4)$$

where the subscripts g, i , and e stand for the gas (meant here as the global flow), ions, and electrons, respectively. We assume an ideal-fluid equation of state (see, e.g., Rezzolla & Zanotti 2013) to calculate the internal energies, i.e., $u_k = p_k/(\tilde{\Gamma}_k - 1)$, where p_k and $\tilde{\Gamma}_k$ are the isotopic pressure and the adiabatic index of the species ($k = g, i, e$). In a realistic scenario, the temperatures of the components are different in different parts of the simulation domain and also vary during the dynamic evolution of the flow. Consequently, the adiabatic indices should also change following the relativistic equation of state (Chandrasekhar 1939; Sygne 1957). For simplicity, we consider constant adiabatic indices that are constant in space and time for the electrons, ions, and the gas as a whole. Indeed, considering temperature-dependent adiabatic indexes, Sądowski et al. (2017) have shown that $\tilde{\Gamma}_e$ is always of the order of $\sim 4/3$ and that since the ion temperature is normally $T_i \lesssim 10^{11.5}\text{K}$, – so that the ions can be considered as non-relativistic – it is reasonable to assume $\tilde{\Gamma}_i \sim 5/3$. Also, since Sądowski et al. (2017) report that the adiabatic index of the flow varies between $5/3$ (in the disk midplane) and $4/3$ (in the polar region), we decide to set $\tilde{\Gamma}_e = 4/3$ and $\tilde{\Gamma}_i = 5/3$, and $\tilde{\Gamma}_g = 13/9$ as for a gas that is thermally trans-relativistic (e.g., Shiokawa et al. 2012; Ryan et al. 2017, 2018).

From the pressure of the individual components, we can calculate the corresponding temperatures T_k assuming an ideal-gas law, i.e., $p_k = \rho k_B T_k / m_k$, where k_B is the Boltzmann constant and m_k is the mass of k -th components of the flow. Using these temperatures and other flow variables, we can calculate the dissipative-heating fraction, the Coulomb-interaction rate, and radiation-cooling rates as detailed below. More specifically, we consider a turbulent-heating prescription to determine the fraction of dissipative heating f . To model this quantity, we follow the results of numerical simulations by Howes (2010, 2011). In particular, the fraction f is simply defined

as

$$f := \frac{1}{1 + Q_i/Q_e}, \quad (5)$$

where

$$\frac{Q_i}{Q_e} = c_1 \frac{c_2 + \beta^\alpha}{c_2 + \beta^\alpha} \sqrt{\frac{m_p T_i}{m_e T_e}} \exp(-1/\beta),$$

where m_e and m_p refer to the mass of electron and proton, respectively, while $c_1 = 0.92$, $c_2 = 1.6/(T_i/T_e)$, $c_3 = 18 + 5 \log(T_i/T_e)$, $\alpha = 2 - 0.2 \log(T_i/T_e)$, and $\beta = p_{\text{gas}}/p_{\text{mag}}$. Next we express the Coulomb interaction and radiation-cooling terms used in Eqs. (2)–(3) in CGS units. Finally, we convert these terms to the units adopted by the code before returning to Eq. (2)–(3) as $\Lambda = Q^-/U_c$ and $\Lambda_{ei} = Q_{ei}/U_c$, where $U_c = \dot{M}_{\text{cgs}} c^2 / r_g^3$ and \dot{M}_{cgs} is the mass-accretion rate (\dot{M}) in CGS units. Accordingly, we express the Coulomb-interaction rate (Q_{ei}) following Spitzer (1965); Colpi et al. (1984), whose explicit form in CGS units is given by

$$Q_{ei} = 1.6 \times 10^{-13} \frac{k_B \sqrt{m_e} \ln \Lambda_0}{m_p} n_e n_i (T_i - T_e) T_e^{-3/2}, \quad (6)$$

where we consider $\ln \Lambda_0 = 20$.

In order to calculate the Bremsstrahlung-cooling rate, we follow the prescriptions reported by Esin et al. (1996). More precisely, the free-free Bremsstrahlung-cooling rate for an ionised plasma consisting of electrons and ions is given by $Q_{\text{br}} = Q_{\text{br}}^{\text{ei}} + Q_{\text{br}}^{\text{ee}}$, where the explicit forms of the individual terms are

$$Q_{\text{br}}^{\text{ei}} = 1.48 \times 10^{-22} n_i n_e \times \begin{cases} 4 \sqrt{\frac{2\Theta_e}{\pi^3}} \left(1 + 1.781\Theta_e^{1.34}\right), & \text{if } \Theta_e < 1 \\ \frac{9\Theta_e}{2\pi} (\ln(1.123\Theta_e) + 0.48) + 1.5, & \text{otherwise.} \end{cases} \quad (7)$$

and

$$Q_{\text{br}}^{\text{ee}} = \begin{cases} 2.56 \times 10^{-22} n_e^2 \Theta_e^{3/2} \left(1 + 1.1\Theta_e + \Theta_e^2 - 1.25\Theta_e^{5/2}\right), & \text{if } \Theta_e < 1 \\ 3.24 \times 10^{-22} n_e^2 \Theta_e (\ln(1.123\Theta_e) + 1.28), & \text{otherwise.} \end{cases} \quad (8)$$

Here, $\Theta_e := k_B T_e / m_e c^2$ is the dimensionless electron temperature.

Because of the presence of a strong magnetic field, the hot electrons in the accretion flow radiate via the thermal synchrotron process. We consider the rate of synchrotron emission (Esin et al. 1996) as follows

$$Q_{\text{cs}} = \frac{2\pi k_B T_i v_c^3}{3Hc^2} + 6.76 \times 10^{-28} \frac{n_e}{K_2 (1/\Theta_e) a_1^{1/6}} \times \left[\frac{1}{a_4^{11/2}} \Gamma\left(\frac{11}{2}, a_4 v_c^{1/3}\right) + \frac{a_2}{a_4^{19/4}} \Gamma\left(\frac{19}{4}, a_4 v_c^{1/3}\right) + \frac{a_3}{a_4^3} \left(a_4^3 v_c + 3a_4^2 v_c^{2/3} + 6a_4 v_c^{1/3} + 6\right) \exp(-a_4 v_c^{1/3}) \right], \quad (9)$$

where H is the local scale-height, which we estimate from the gradient of the electron temperature is calculated by $H = T_e^4 / |\nabla T_e^4|$ (Fragile & Meier 2009) and finally, K_2 is the modified Bessel function of the second kind. The coefficients a_{1-4} in expression (9) have explicit expressions

$$a_1 = \frac{2}{3v_0\Theta_e^2}, \quad a_2 = \frac{0.4}{a_1^{1/4}}, \quad a_3 = \frac{0.5316}{a_1^{1/2}}, \quad a_4 = 1.8899a_1^{1/3}, \quad (10)$$

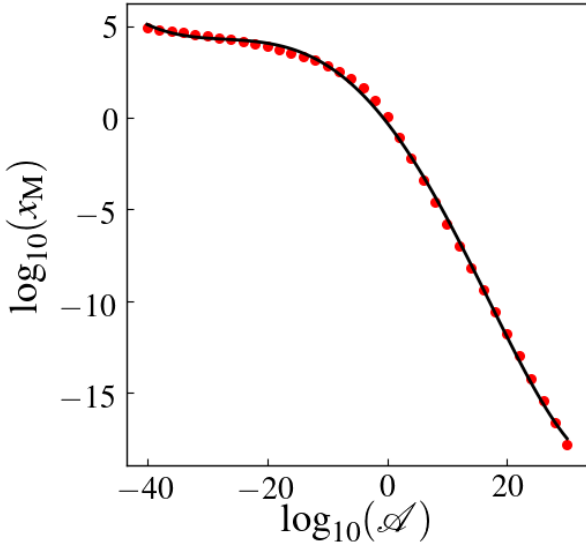


Figure 1. Plot of quantity $x_M := 2\nu/(3\nu_0\Theta_e^2)$ appearing in Eq. (14) shown as a function of the variable \mathcal{A} . The numerical solution is shown by the red dots line while its polynomial fit is shown with the black solid line.

while Γ is the ‘‘Gamma function’’, namely, $\Gamma(a, x) := \int_x^\infty t^{a-1} e^{-t} dt$. Additionally, $\nu_0 := eB/(2\pi m_e c)$ and ν_c are the characteristic synchrotron frequencies, where e and B refer to the electronic charge and the magnetic field strength in CGS units, respectively. The characteristic synchrotron frequencies can be calculated by equating the emissivities of optically thin and thick volumes (Esin et al. 1996),

$$\frac{e^2}{c\sqrt{3}} \frac{4\pi\nu_c n_e}{K_2(1/\Theta_e)} I'(x_M) = \frac{2\pi k_B T_e}{Hc^2} \nu_c^2, \quad (11)$$

with

$$I'(x_M) = \frac{4.05}{x_M^{1/6}} \left(1 + \frac{0.4}{x_M^{1/4}} + \frac{0.5316}{x_M^{1/2}} \right) \exp(-1.8899x_M^{1/3}), \quad (12)$$

and where $x_M := 2\nu_c/(3\nu_0\Theta_e^2)$. For simplicity, we rewrite Eq. (11) as

$$I'(x_M) = \mathcal{A} x_M, \quad (13)$$

where

$$\mathcal{A} := \frac{2\sqrt{3}\pi m_e c \Theta_e K_2(1/\Theta_e)}{4e^2 n_e H} \frac{3\nu_0 \Theta_e^2}{2} \sim \frac{3\sqrt{3}}{4} \frac{m_e c}{e^2} \frac{\Theta_e^5 \nu_0}{n_e H}, \quad (14)$$

and where we consider $K_2(1/\Theta_e) \sim \Theta_e^2$. We numerically solve Eq. (13) for x_M for all possible values of \mathcal{A} within the range $[10^{-40}, 10^{30}]$. Subsequently, we fit the solutions with a polynomial of fifth-order as follows

$$\log_{10}(x_M) = A_0 + A_1 \log_{10}(\mathcal{A}) + A_2 (\log_{10}(\mathcal{A}))^2 + A_3 (\log_{10}(\mathcal{A}))^3 + A_4 (\log_{10}(\mathcal{A}))^4 + A_5 (\log_{10}(\mathcal{A}))^5, \quad (15)$$

where $A_0 = -0.273264$, $A_1 = -0.421236$, $A_2 = -0.0108989$, $A_3 = 4.24618 \times 10^{-5}$, $A_4 = 4.33030 \times 10^{-6}$, and $A_5 = 2.35786 \times 10^{-8}$. The comparison of the numerical solutions (dots) and the polynomial fit (solid line) is shown in Fig. 1 and clearly indicates the quality of the fit. Interestingly, this approach effectively reduces the computational costs of about four orders of magnitude.

It is important to remark that Eq. (9) is appropriate only in the

Model	Physical processes	M/\dot{M}_{Edd} \log_{10}
T	Turbulent heat.	-4
TC	Turbulent heat. + Coulomb heat.	-4
TCR-A	Turbulent heat. + Coulomb heat. + Radiative cool.	-4
TCR-B	Turbulent heat. + Coulomb heat. + Radiative cool.	-5
TCR-C	Turbulent heat. + Coulomb heat. + Radiative cool.	-6
TCR-D	Turbulent heat. + Coulomb heat. + Radiative cool.	-8
TCR-DM	Turbulent heat. + Coulomb heat. + Radiative cool.	-8
TCR-E	Turbulent heat. + Coulomb heat. + Radiative cool.	-11

Table 1. List of the various models considered in the simulations alongside with the microphysical processes that are taken into account. Also reported for the different models are the accretion rates expressed in terms of the Eddington accretion rate \dot{M}_{Edd} .

presence of thermal electrons. In order to ensure that the contribution to the thermal synchrotron radiation from the highly-magnetised region is negligible, we modify (9) with the help of a cutoff value for the magnetisation σ , namely, the ratio between rest-mass and magnetic energy densities: $\sigma := b^2/\rho$. More specifically, we set $Q'_{\text{cs}} = \exp(-(\sigma/\sigma_{\text{cut}})^2) Q_{\text{cs}}$ with $\sigma_{\text{cut}} = 10$.

In addition, we also incorporate the Comptonization of synchrotron radiation. In our simplified model, we calculate the Compton-enhancement factor of the synchrotron radiation at the local cutoff frequency (ν_c). In this way, the total radiation-cooling rate is calculated as

$$Q^- = Q_{\text{br}} + \eta(\nu_c) Q'_{\text{cs}}, \quad (16)$$

where η is the Compton enhancement factor, whose explicit expression is (Narayan & Yi 1995)

$$\eta(\nu_c) = 1 + \frac{P(A-1)}{1-PA} \left(1 - \left(\frac{3k_B T_e}{h\nu_c} \right)^{\eta_1} \right), \quad (17)$$

with, $P = 1 - \exp(-\tau_{\text{es}})$, $A = 1 + 4\Theta_e + 16\Theta_e^2$, $\eta_1 = 1 + \ln P/\ln A$, and $\tau_{\text{es}} = 2\sigma_{\text{T}} n_e H$, where σ_{T} is the Thomson cross section of the electron.

2.2 Model setup

We initialise our simulations of magnetised tori with an axisymmetric torus in pressure equilibrium (Fishbone & Moncrief 1976) with parameters $r_{\text{in}} = 6r_g$ and $r_{\text{max}} = 12r_g$, where r_{in} and r_{max} are the inner radius and the radius of the pressure maximum of the torus, respectively. Given this combination of parameters, the subsequent flow leads to a SANE accretion flow. In a SANE flow, the magnetic field strength is weak and merely serves as a mechanism to transport angular momentum (e.g., Narayan et al. 2012; Porth et al. 2017; Nathanail et al. 2020). However, for completeness, we have also considered a MAD accretion modes (i.e., model TCR-DM), which is triggered by a torus with $r_{\text{in}} = 20r_g$ and $r_{\text{max}} = 40r_g$. In a MAD flow, by contrast, the magnetic field is strong enough to govern the dynamics of the flow (e.g., Tchekhovskoy et al. 2011; Narayan et al. 2012). In all cases, the magnetic field is introduced via a weak poloidal single-loop¹ magnetic field specified via a vector potential A_μ . More

¹ We note that a multi-loop initial magnetic-field configuration has also been considered and shown to lead to a different and interesting phenomenology that has potential applications in understanding flaring activities in the supermassive black hole, e.g., Sgr A* (Nathanail et al. 2020)

specifically, given the symmetries adopted in our set-up, the vector potential has only one non-zero component $A_\phi \propto \max(q, 0)$, where

$$q = \begin{cases} \rho/\rho_{\max} - 0.2, & \text{for SANE} \\ \rho/\rho_{\max} (r/r_{\text{in}})^3 \sin^3 \theta \exp(-r/400) - 0.01, & \text{for MAD.} \end{cases} \quad (18)$$

The strength of the initial magnetic field is determined by the specified initial value of the maximum plasma- β parameter, $\beta_{\max} = \rho_{\text{gas}}/\rho_{\text{mag}}|_{\max}$, which is specified at the location of the rest-mass density maximum in the torus. For this study, we consider $\beta_{\max} = 100$ for all simulation models and perform all the simulations in spherical modified Kerr-Schild coordinates in two dimensions (axisymmetric) (r, θ) (McKinney & Gammie 2004). The simulation domain extends radially from well inside the black-hole event horizon to $r = 2500 M_\bullet$ using a logarithmic spacing. In the polar direction, we consider the domain ranges from a polar angle $\theta = 0$ to $\theta = \pi$ with uniform spacing. The numerical domain is resolved with an effective grid resolution of 2048×1024 and with three AMR levels. Furthermore, we set no-inflow boundary conditions at the radial boundaries of the numerical domain. In contrast, we set the scalar variables and the radial component of vectors to be symmetric at the polar boundaries, while the azimuthal and polar vector components are set to be antisymmetric at the polar boundaries.

In order to excite the magneto-rotational instability (MRI), we initially apply a 1% random perturbation to the gas pressure within the torus. As it is customary in Eulerian, finite-volume codes, we adopt a floor model to ensure that the GRMHD code can handle the low-density regions, particularly close to the black hole and the rotation axis (Rezzolla & Zanotti 2013). More specifically, we set the floor rest-mass density and pressure as $\rho_{\text{fl}} = 10^{-4} r^{-3/2}$ and $p_{\text{fl}} = (10^{-6}/3) r^{-5/2}$, respectively. In the case of the electron pressure, we set $p_e = 0.01 p_{\text{fl}}$ for $p_e \leq 0.01 p_{\text{fl}}$ and $p_e = 0.99 p_{\text{fl}}$ for $p_e \geq 0.99 p_{\text{fl}}$. Note that we recalculate the entropy of the gas (κ_g) and of the electrons (κ_e) in the numerical cells where the flooring is needed. In all simulations, we fix the mass and spin of the black hole to be $M_\bullet = 4.5 \times 10^6 M_\odot$ and $a_* = 0.9375$, respectively.

To obtain a rather broad and comprehensive investigation of the various scenarios, we consider several simulation models, where details of these models are summarised in Table 1. More specifically, models T, TC, and TCR-A are devised to study the impacts of included physics in combination with turbulent heating (T), Coulomb interaction (C), and radiative cooling (R). Furthermore, in order to understand the role played by the accretion rate in the thermodynamics of electrons, we consider models TCR-A, B, C, D, and E with different values of the mass-accretion rate, namely $\dot{M} = 10^{-4} - 10^{-11} \dot{M}_{\text{Edd}}$, where $\dot{M}_{\text{Edd}} = 1.4 \times 10^{17} M_\bullet/M_\odot$ is the Eddington mass-accretion rate. Finally, model TCR-DM is designed to study the difference in the electron thermodynamics between the SANE (model TRC-D) and the MAD accretion flows. Before moving to the results, we recall that GRMHD simulations not involving radiative-transfer processes are independent of the black-hole mass, which can be therefore simply rescaled. On the other hand, when radiative-transfer is taken into account, the results do depend on the mass of the black hole since the radiative processes depend on the mass-accretion rate. In view of this, in our simulations we keep the black-hole mass fixed and vary only the mass-accretion rate.

3 RESULTS

To illustrate the temporal properties of the accretion flow, we show in Fig. 2 the profile of the mass-accretion rate ($\dot{M}/\dot{M}_{\text{Edd}}$) and of the

magnetic-flux rate at the black hole horizon ($\Phi_{\text{BH}}/\sqrt{\dot{M}}$) for different simulation models: T (black), TC (blue), TCR-A (green), TCR-D (red), TCR-DM (magenta). The grey line in the Fig. 2b corresponds to $\Phi_{\text{BH}}/\sqrt{\dot{M}} = 15$, which is commonly adopted as the threshold in the magnetic-flux rate distinguishing SANE accretion ($\Phi_{\text{BH}}/\sqrt{\dot{M}} < 15$) from MAD accretion modes ($\Phi_{\text{BH}}/\sqrt{\dot{M}} > 15$; details on how these quantities are calculated have been reported by Porth et al. (2017).

As it is well-known in these simulations, the weak poloidal magnetic field lines wind up as the evolution proceeds and generate the toroidal component. The differential rotation in the torus triggers the MRI, which helps in the outward transport of angular momentum, triggering and regulating the accretion process. Further, the MRI also amplifies the toroidal component of the magnetic field (e.g., Begelman & Pringle 2007). We set the effective resolution such that the fastest growing MRI mode is resolved with a quality factor $Q_\theta \gtrsim 6$, except for the very high-density region for the SANE modes (see, e.g., Fig. 13 of Nathanail et al. 2020, for a representative example), which is required to ascertain that MRI is active in our simulations (e.g., Sano et al. 2004). Once the accretion process is set, we observe that the mass-accretion rates for all the simulation models (T, TC, TCR-A, TCR-D) reach a quasi-steady-state after a certain time $t \gtrsim 1500 M_\bullet$, except for model TCR-DM, which reaches a quasi-steady-state after $t \gtrsim 2500 M_\bullet$ as a result of the larger inner radius of the torus r_{in} (see Fig. 2a).

After $t \gtrsim 4000 M_\bullet$, the mass-accretion rate and the magnetic-flux rates for model TCR-DM show the large oscillations that are typical of the MAD accretion mode and that reflect the periodic quenching of the accretion flow close to the black hole (e.g., Tchekhovskoy et al. 2011; Dihingia et al. 2021). Also, in Fig. 2b, we observe that with time, $\Phi_{\text{BH}}/\sqrt{\dot{M}}$ increases and reaches a maximum value. Except for model TCR-DM (magenta), the value of $\Phi_{\text{BH}}/\sqrt{\dot{M}}$ drops at time $t \sim 1500 M_\bullet$ and saturates after $t \gtrsim 5000 M_\bullet$, with $\Phi_{\text{BH}}/\sqrt{\dot{M}} \sim 1.5$. The profiles of $\Phi_{\text{BH}}/\sqrt{\dot{M}}$ essentially suggest that all these simulation models are in the SANE state. The only exception is for model TCR-DM, where the magnetic-flux rate at the black hole horizon increases monotonically and exceeds the saturation limit for a MAD configuration after $t \gtrsim 4000 M_\bullet$, i.e., $\Phi_{\text{BH}}/\sqrt{\dot{M}} \sim 15$ (e.g., Tchekhovskoy et al. 2011; Mizuno et al. 2021). We recall that in a MAD accretion mode, the inner part of the accretion flow releases a substantial amount of the accumulated magnetic flux through magnetic eruption events (e.g., Igumenshchev 2008; Dexter et al. 2020b; Porth et al. 2021). When this happens, the magnetic flux drops to a smaller value ($\Phi_{\text{BH}}/\sqrt{\dot{M}} \ll 15$) up until sufficient magnetic flux is advected by the flow and accumulates near the horizon, leading to a MAD cycle with an increase in the magnetic-flux rate. This process continues in the form of quasi-period oscillations throughout the simulation time. Note that in more realistic three-dimensional (3D) GRMHD simulations, the eruption events in MAD configuration are not as abrupt as seen in Fig. 2. The profile for $\Phi_{\text{BH}}/\sqrt{\dot{M}}$ for the MAD regime in 3D GRMHD simulations is much more laminar compared to asymmetric models with episodic eruption events due to the presence of interchange instabilities in the azimuthal direction (e.g., see Mizuno et al. 2021; Dexter et al. 2020b; Porth et al. 2021).

During the quasi-steady-state, we observe various phenomena driven by turbulence, reconnection events, plasmoids, and so on. These features are qualitatively similar to the studies done in the single-fluid ideal GRMHD framework (e.g., Porth et al. 2017, 2019; Nathanail et al. 2020; Dihingia et al. 2021; Porth et al. 2021). However, since the main interest in our investigation is the study of the time-averaged properties of the accretion flow, we will not discuss in detail the properties of the plasma – which can be found well de-

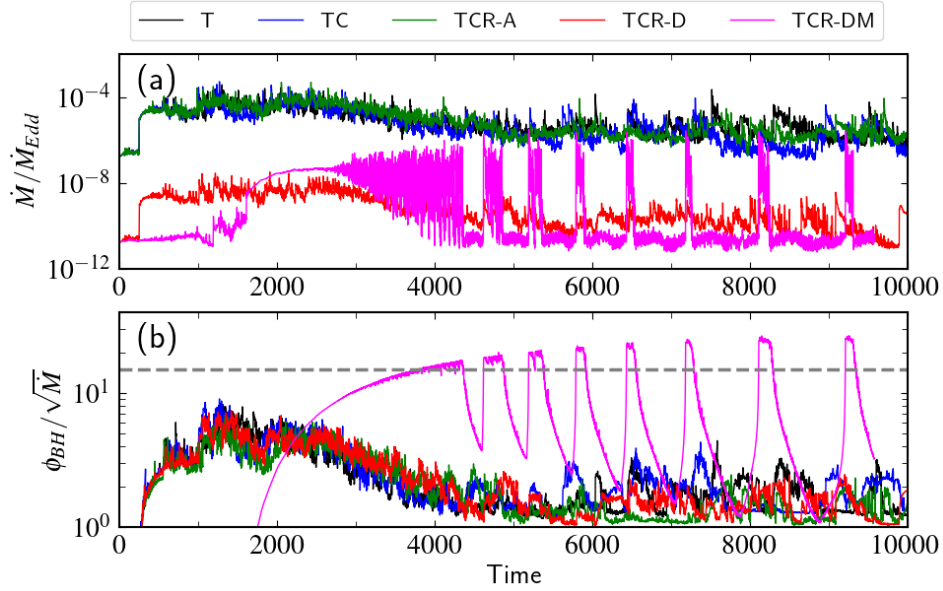


Figure 2. Evolution of the mass-accretion rate $\dot{M}/\dot{M}_{\text{Edd}}$ as measured at the event horizon (top panel) and of the corresponding normalised magnetic flux $\phi_{\text{BH}}/\sqrt{\dot{M}}$. The horizontal gray dashed line corresponds to $\phi_{\text{BH}}/\sqrt{\dot{M}} = 15$ and marks therefore the threshold for a MAD accretion mode.

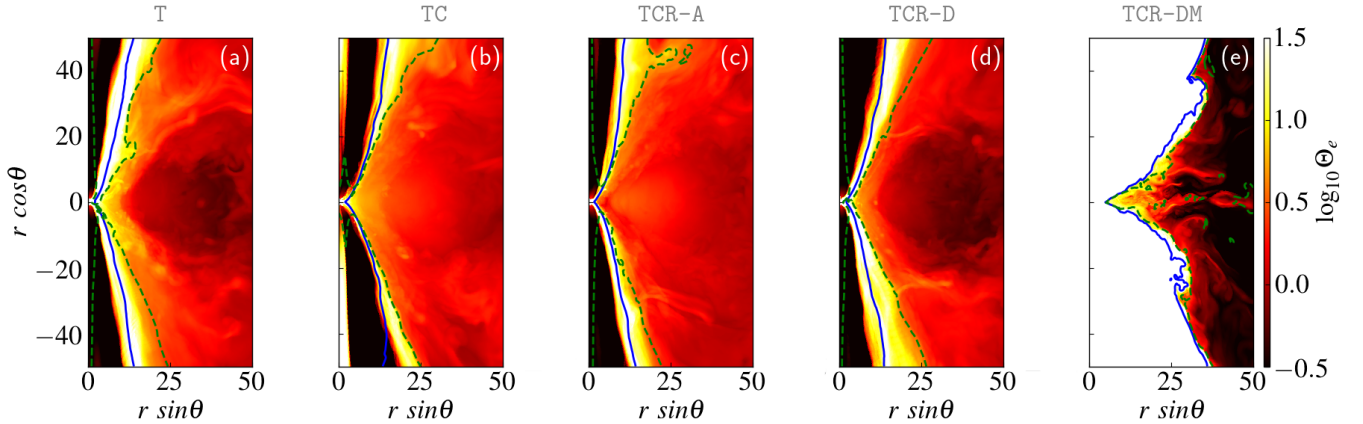


Figure 3. Spatial distributions of the dimensionless electron temperatures Θ_e for the different simulation models: T, TC, TCR-A, TCR-D, and TCR-DM [panels (a), (b), (c), (d), and (e), respectively]. The distributions are time-averaged within the window $t = 8000 - 9000 M_\bullet$, and the blue solid and green dashed lines mark the boundaries where $\sigma = 1$ and the Bernoulli parameter $-hu_t = 1$, respectively.

scribed in the references above – and concentrate instead on a number of time-averaged flow quantities. We should also note that our simulations treat the accretion flow only at low accretion rates, which remains optically thin. Under these conditions, the radiative-cooling processes are not strong enough to collapse the geometrically thick torus to a thin-disc structure.

3.1 Distribution of the temperatures

In Figs. 3 and 4, we show the time-averaged and dimensionless electron temperature Θ_e and the dimensionless ion temperature $\Theta_i := k_B T_i / m_p c^2$ for the simulation models T, TC, TCR-A, TCR-D, and TCR-DM (the names of various models are reported at the top of each panel), within a temporal domain $t = 8000 - 9000 M_\bullet$. Each panel shows the distribution in a small region near the black hole, with the blue-solid and the green-dashed lines indicating the contours

with magnetisation $\sigma = 1$ and a Bernoulli parameter $-hu_t = 1$, respectively, where h is the specific enthalpy of the flow. The region around the rotation axis of the black hole with $\sigma > 1$ and $-hu_t > 1$ is known as the funnel region of the flow.

The region surrounding the polar funnel contributes to the wind from the disc, which is also known as the jet-sheath region of the flow. In Fig. 3a (model T), electrons receive a fraction of the energy gained by the flow via the turbulent heating. As a result, we observe a higher electron temperature in the region close to the black hole and in the jet-sheath region. We note that such an efficient electron heating around the shearing region between bound and unbound material ($-hu_t \sim 1$, green dashed contour) was reported by also by several previous studies (e.g., Chael et al. 2019; Dexter et al. 2020a; Anantua et al. 2020; Mizuno et al. 2021).

With the inclusion of the Coulomb-interaction term (panel 3b, model TC), the electrons gain an extra fraction of energy from the ion

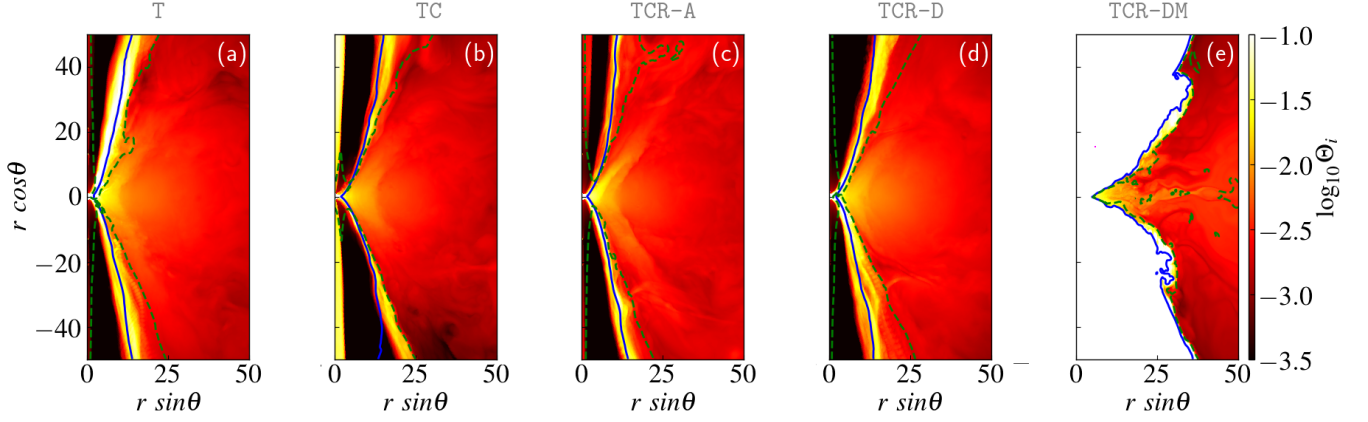


Figure 4. Same as in Fig. 3 but for the time-averaged dimensionless ion temperature Θ_i

fluid. Consequently, the electron temperature becomes even higher for model TC throughout the domain as compared to model T. If the electrons are allowed to cool through the radiation-cooling processes (model TCR-A, panel (c) in Fig. 3), the electron temperature then decreases in the region close to the black hole (see the dark red colour) when compared to models TC and T. Furthermore, when the mass-accretion rate is set to be smaller (model TCR-D, panel (d) in Fig. 3), the overall density of the flow and the magnetic-field strength decrease as compared to the higher accretion rate cases. Consequently, the radiative cooling due to the Bremsstrahlung and the synchrotron processes becomes less efficient. On the contrary, the turbulent heating process remains unaffected as it depends only on the plasma- β and the ratio of temperatures. These quantities suffer minimum changes due to the decrease in accretion rate. Therefore, the electrons remain hot close to the black hole and in the jet-sheath region. Also, together with the decrease of the accretion rate, the Coulomb-interaction rate decreases, so that the electrons in the high-density region are comparatively cooler when compared to the high accretion flow (model TCR-A, panel (c) in Fig. 3).

The effects of the radiative cooling and of the heating in the SANE and MAD accretion modes can be appreciated by comparing panels (d) and (e) in Fig. 3. More specifically, in the MAD mode (model TCR-DM), the turbulent heating dominates in the polar region, resulting in a very hot funnel with temperatures that are considerably higher, i.e., more than a factor of $\sim 10 - 50$, than in the SANE mode (model TCR-D). However, in the high-density regions, the electrons are actually colder in the MAD mode and by a factor $\sim 3 - 5$. Note that in both cases the electrons remain hot close to the black hole, since the Coulomb-interaction term dominates over the radiative cooling in these regions.

Figure 4 reports the distribution of the ion temperature for the different models considered and effectively shows the impact of the Coulomb-interaction term on this quantity. Note that the Coulomb interaction actually acts as a cooling term for the ions. As a result, with its inclusion, the ions close to the black hole and the jet-sheath region are significantly colder (compare panels (a) and (b) of Fig. 4). Since the electrons are allowed to cool through radiative cooling, the difference between the electron and ion temperatures increases, and as a result, the efficiency of the Coulomb interaction also increases (see Eq. 6), leading to a cooling of the ions in the high-density region (see panel (c) in Fig. 4). With the decrease of the accretion rate (see panel (d) in Fig. 4), the efficiency of both the radiative cooling and the

Coulomb interaction drops. As a result, the ions in the high-density region remain hotter than in the highly accreting cases (Fig. 4c). Furthermore, by comparing panels (d) and (e) of Fig. 4, it is possible to note that the ions in the funnel region are hotter for the MAD mode than in the SANE mode for the same accretion rate. At the same time, the ions in the high-density region are colder in the MAD accretion mode than in the SANE accretion mode.

To better understand the contribution of the heating and cooling terms, we report in Fig. 5 the distribution of the temperature ratio T_e/T_i averaged over a time window of $t = 8000 - 9000 M_\bullet$ and for all of the different models considered in Figs. 3 and 4. We note that for the model with only turbulent heating (model T, Fig. 5a), we observe that the heating of the electrons is particularly strong in the jet-sheath region, where $-hu_t \sim 1$ and $T_e/T_i \sim 1 - 10$. However, in the funnel region, the electrons remain cold, i.e., $T_e/T_i \lesssim 0.01$. With the inclusion of the Coulomb-interaction term, the electrons heat up and consequently, the ratio T_e/T_i increases throughout the domain, except in the funnel region (see panel (b) in Fig. 5); this is because the electron-ion collision rate is suppressed in these regions as a result of the very low density, so that ions cannot transfer their energy to the electrons.

We note that when the radiative cooling is included (panels (c) and (d) in Fig. 5), it overpowers the heating processes close to the black hole, resulting in a lower value of T_e/T_i there. When comparing the SANE and MAD accretion modes (panels (d) and (e) in Fig. 5), it is possible to note that the distribution of T_e/T_i is different in the jet-sheath and in the funnel regions. More specifically, in the MAD mode, both the electron and ion temperatures around the equatorial plane and far from the black hole are smaller than those encountered in the SANE mode (see Figs. 3 and 4). On the contrary, near the black hole, the behaviour is the opposite. To understand the origin of this difference, we report in Fig. 6 the ratio T_e/T_i as a function of the polar angle (θ) at different radii close to the black hole for both the SANE (left panel) and the MAD (right panel) simulations. The two panels essentially suggest that for the SANE modes, the ratio $T_e/T_i \lesssim 1$ in the jet-sheath and the ratio $T_e/T_i \lesssim 0.1$ in the funnel region. However, for the MAD mode, the ratio $T_e/T_i \gtrsim 1$ in both the jet-sheath and funnel. Earlier studies with turbulent heating also suggest that a hot funnel flow develops in the case of MAD accretion modes (Dexter et al. 2020a; Mizuno et al. 2021). We should note that we consider the SANE models to have a magnetic flux ~ 10 times smaller than the MAD model (see Fig. 2). In principle, we can raise the magnetic flux

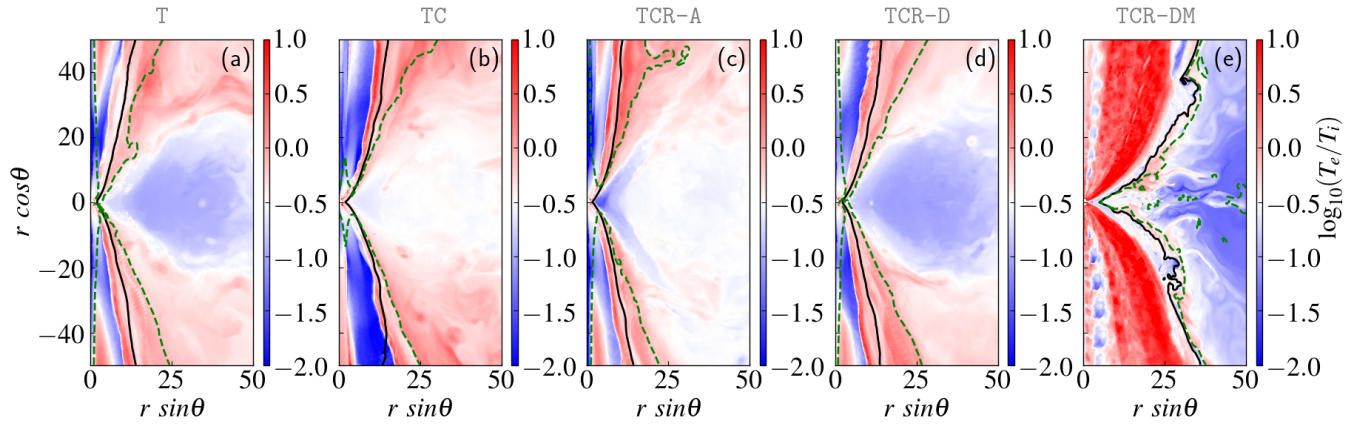


Figure 5. Ratio of the time-averaged electron-to-ion temperatures T_e/T_i (see Figs. 3 and 4). The black solid and green dashed lines mark the boundaries where $\sigma = 1$ and the Bernoulli parameter $-hu_t = 1$, respectively.

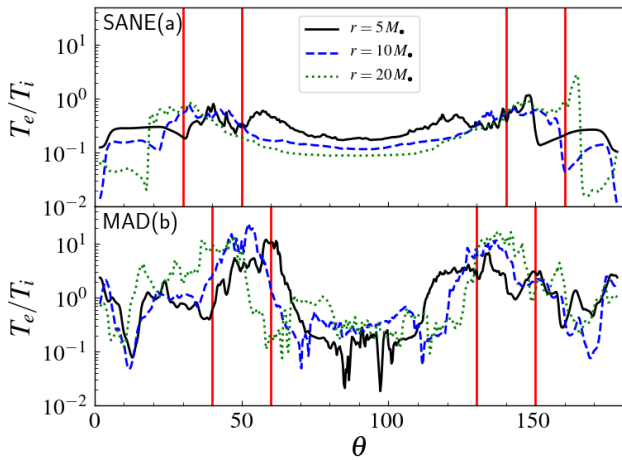


Figure 6. Plots of temperature ratio T_e/T_i shown as a function of the polar angle θ (in degrees) at different radii $r = 5, 10, 20 M_\bullet$ for models TCR-D (top panel) and TCR-DM (bottom panel). The two vertical red lines on both sides of the equatorial plane ($\theta = 90$) roughly denote the jet-sheath region; regions the left or to the right of these two lines correspond to the funnel.

accumulation around the event horizon of a black hole by setting the initial condition of the accretion flows such as torus size and initial magnetic field strength. If the normalised magnetic flux is still within the SANE limit (e.g., $\Phi/\sqrt{M} \sim 5 - 10$), the accretion flow is still referred to as SANE. However, the temperature profiles of electrons and ions may not be as distinct as stated in this study.

3.2 Correlation of the temperatures

In order to fully understand the correlation between the temperatures, we collect the ratio of the temperatures T_e/T_i and T_e/T_g from all the grid-cells in the computational domain with $r < 100 M_\bullet$. The distribution of the corresponding temperature ratios T_e/T_i and T_e/T_g as a function of the plasma- β is shown in the top and bottom panels of Fig. 7, respectively. In all of the panels of Fig. 7, each dot represents the value measured in a given grid-cell over a time window $t = 8000 - 9000 M_\bullet$. The black dots are collected from the parts of the domain with $\sigma < 1$ and thus corresponding to the “disc region”, while the magenta dots are from cells with $\sigma > 1$ and thus can

Model	$R_{1,p}$	$R_{2,p}$	$R_{3,p}$	β_{br}
T	2.55	1.36	8.52	49.7
TC	2.37	0.89	2.72	8.24
TCR-A	2.05	9.49	-5.54	10.1
TCR-B	2.56	3.24	3.60	18.1
TCR-C	2.78	1.94	6.87	38.4
TCR-D	2.80	1.68	8.59	55.0
TCR-DM	4.50	2.26	22.9	517
TCR-E	2.81	1.52	9.31	55.8

Table 2. Best-fit parameters $R_{1,p}$, $R_{2,p}$, $R_{3,p}$, and β_{br} for the different simulation models. These values are obtained from the time-averaged temperature ratios T_e/T_i over a time window $t = 8000 - 9000 M_\bullet$.

be considered the “jet region”. Note that how in the case of a SANE accretion mode, i.e., for panels (a)–(d) in Fig. 7, these magenta values are mostly restricted to small values of the plasma- β parameter; on the other hand, for a MAD accretion mode, i.e., for panels (e), they can also be associated with values of $\beta \lesssim 10^2$, although they tend to be absent in the regions with $\beta \gg 1$.

Note how the different scatterings of the dots clearly show the impact of various mechanisms on the temperatures. In particular, the inclusion of the Coulomb-interaction term heats-up the electrons quite irrespective of the plasma- β (see panels (a) and (b) of Fig. 7). As a result, the value of T_e/T_i increases in the whole range of plasma- β for model TC when compared to model T. The increase in the temperature ratios is prominent for the higher plasma- β range (i.e., $\beta > 10$), as the Coulomb interaction is more efficient in the high-density region of the disc. As we include the radiative-cooling processes (panel (c)), electrons are cooled and lower values of T_e/T_i and T_e/T_g are reached for $\beta \sim 1$. However, in the region with low plasma- β , the turbulent heating remains stronger than the radiation-cooling term and the electrons in these regions remain comparatively hot. Note the appearance of a local minimum in the temperature ratios in panels (c) of Fig. 7, which indicates that the cooling is particularly important and actually dominating in the range $\beta \sim 1 - 10$.

With the decrease in the accretion rate, the efficiency of the Coulomb heating and of the radiative cooling also decreases (panels (d) and (e) of Fig. 7). On the contrary, the rate of turbulent heating is independent of the accretion rate (see Eq. (5)). As a result, electrons with lower plasma- β remain hot while electrons with higher plasma- β remain cold when the accretion rates are small. Interestingly, the ratio T_e/T_i becomes greater than unity in the regions where the tur-

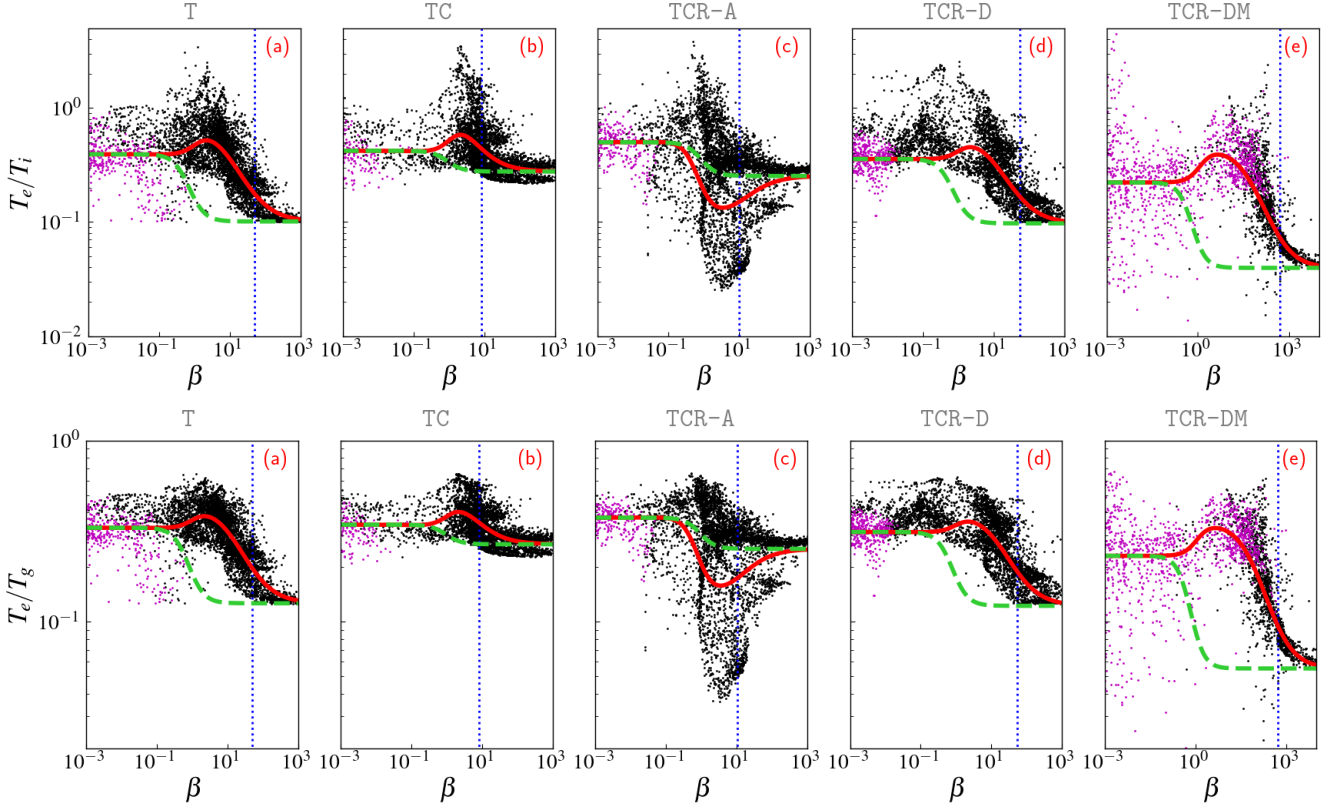


Figure 7. Distributions of the temperature ratio T_e/T_i (top panels) and of T_e/T_g (bottom panels) as a function of plasma- β for the simulation models TCR-A, TCR-D, and TCR-DM [panels (a), (b), and (c), respectively]. Each dot refers to a cell in the computational domain, with the black dots referring to the region with $\sigma < 1$ (roughly representative of the disc) and the magenta dots to the region with $\sigma > 1$ (roughly representative of the jet). The solid red curves corresponds to our new $R - \beta$ relations, while the dashed green lines correspond to the usual $R - \beta$ relation. The vertical dotted blue lines mark the value of $\beta = \beta_{br}$.

bulent heating of electrons is efficient and the radiative cooling is less efficient. These regions appear around the funnel (see Fig. 5). However, the gas temperature always remains higher than that of the electrons throughout the simulation domain (see bottom panels of Fig. 7).

Figure 5 suggests that the ratio T_g/T_e or T_i/T_e shows a broad correlation with the plasma- β parameters. Moreover, the trend of the temperature ratio is quite similar for SANE as well as MAD modes (panels (d) and (e) of Fig. 5). Therefore, it is possible to relate the temperatures ratios T_g/T_e and T_i/T_e with the properties of the plasma- β in the accretion flow. We can do this by fitting the data in Fig 7 with a simple function of plasma- β parameter that can recover the widely used $R - \beta$ prescription in the suitable limits. In particular, we adopt the new ansatz

$$\frac{T_k}{T_e} = \frac{1}{1 + \beta^2} R_{1,k} + \frac{\beta^2}{1 + \beta^2} R_{2,k} + \frac{\beta}{\beta + \beta_{br}} R_{3,k}. \quad (19)$$

where $k = g, i$ and $\beta_{br,k}$ is what we refer to as the “the plasma- β break”, i.e., a characteristic value of the β parameter where the temperature ratio undergoes a sharp change (see below). Two important remarks are needed at this point. First, Eqs. (19) seem to imply that there are six new coefficients $R_{1-3,g}$ and $R_{1-3,p}$; in practice, however, only three are linearly independent since the other three can be derived through relations that are simple to derive in the case of an

ideal-fluid equation of state, namely

$$R_{i,g} = \frac{\tilde{\Gamma}_g - 1}{\tilde{\Gamma}_i - 1} \left(R_{i,p} + \frac{\tilde{\Gamma}_i - 1}{\tilde{\Gamma}_e - 1} \right), \quad i = 1, 2, \quad (20)$$

$$R_{3,g} = \left(\frac{\tilde{\Gamma}_g - 1}{\tilde{\Gamma}_i - 1} \right) R_{3,p}. \quad (21)$$

Second, note that the standard $R - \beta$ relation can be obtained by setting $R_{1,p} = R_{low}$, $R_{2,p} = R_{high}$ and $R_3 = 0$, i.e.,

$$\frac{T_k}{T_e} = \frac{R_{low}}{1 + \beta^2} + \frac{R_{high}\beta^2}{1 + \beta^2}. \quad (22)$$

The new functional form of the temperature ratios (19) is built on the expectation that the electrons should be cooled by the thermal synchrotron emission in the moderately magnetised region with $\beta \sim 1$. In addition, the electrons should have a higher temperature in the highly magnetised regions as a result of the strong turbulent heating. Under these considerations, and for $\beta \ll 1$, the temperature ratios reduce to $T_i/T_e \simeq R_1$ and $T_g/T_e \simeq R_1$. For larger values of β , and depending on the heating and cooling processes, the ratio of the temperatures may increase or decrease. However, for $\beta \gg \beta_{cr} \gg 1$, the temperature ratios tend to reach constant values $T_i/T_e \simeq T_g/T_e \simeq R_{2,p} + R_{3,p}$, so that the standard value of R_{high} normally employed in the standard $R - \beta$ relation (22) is actually given by $R_{high} = R_{2,p} + R_{3,p}$.

In the various panels of Fig. 7 we show with a solid red line the new $R - \beta$ relations (19) as obtained from the best-fit parameters for the various models considered; for the ratio T_i/T_e these best-fit

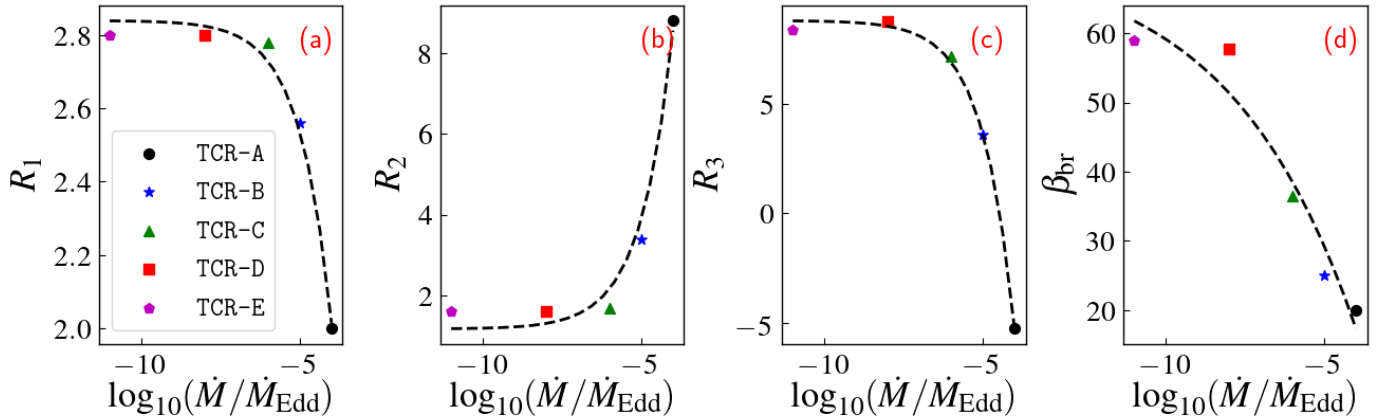


Figure 8. Values of the best-fit parameters $R_{1-3,p}$ and of β_{br} as a function of the accretion rate expressed in CGS units and normalised to the Eddington accretion rate. Different symbols are used to refer to the different models considered, while black dashed lines correspond to the fitting functions of the data.

parameters $R_{1-3,p}$ are reported in Table 2 for the various models considered, while for the T_g/T_e ratio they can be obtained by using expressions (21). In all of the panels of Fig. 7 we also show the value of β_{br} with a vertical blue dotted line. Note that the new $R-\beta$ relation broadly follows the trend of the ratio of the temperatures as a function of the plasma- β of the fluid. For comparison, in Fig. 7, we also overlay the standard $R-\beta$ function with $R_{\text{low}} = R_1$ and $R_{\text{high}} = R_2 + R_3$ with a green dashed line. As expected, the standard $R-\beta$ relation shows a good agreement in the range $\beta \lesssim 0.1$ and $\beta \gtrsim 100$ for all of the models considered, in the range of $0.1 \lesssim \beta \lesssim 100$, it does not provide an accurate description of the thermodynamics of the accreting flow. We note that these three different regions in the plasma- β correspond to spatially different regions, namely, the funnel/shearing region ($\beta \lesssim 0.1$), the jet-sheath region ($0.1 \lesssim \beta \lesssim 100$) and the high-density disc region ($\beta \gtrsim 100$). As a result, the distributions illustrated in Fig. 7 clearly indicate that the standard $R-\beta$ relation does not provide a faithful description of the electron temperature in the jet-sheath region and that it tends to systematically underestimate it; the only exception is for model TCR-A, where a slight overestimate is present in the cooling dominated regions.

Before concluding this section, we note that it is interesting to investigate if the new values of the $R_{1-3,p}$ coefficients provided in Table 2 show some correlation with other bulk properties of the flow, most importantly with the mass-accretion rate. To this scope, we report in Fig. 8, the values of $R_{1-3,p}$ and of β_{br} as a function of the accretion rate normalised to the Eddington accretion rate. Each point in the figure refers to a specific simulation, as indicated in the legend, and the reported values of the $R_{1-3,p}$ parameters represent the best-fits of the distributions of the temperature ratios reported in Fig. 7 and which, we recall, are time-averaged over the window $t = 8000 - 9000 M_\bullet$. A brief inspection of Fig. 8 clearly shows that the best-fit parameters correlate very well with the mass-accretion rate, and in principle, analytic fitting functions can be computed (see black dashed lines in Fig. 8). The explicit forms of the fitting functions are reported in Appendix A. These functions are important to show the correlation of the $R_{1-3,p}$ or β_{br} with the accretion rate. However, one must note that we obtained these functions by computing best-fit parameters and accumulated errors may be significant during this process. Nonetheless, these functions provide ranges of these parameters ($R_{1-3,p}, \beta_{\text{br}}$) at different accretion rates for SANE models.

Note that the values of the parameters change drastically as the accretion rate is higher than a certain value, namely, $\dot{M} \gtrsim 10^{-7} \dot{M}_{\text{Edd}}$. This behaviour suggests that the contribution of the heating and cooling to the thermodynamics of electrons and ions becomes significant for accretion rates $\dot{M} \gtrsim 10^{-7} \dot{M}_{\text{Edd}}$. More importantly, since the standard coefficient R_{high} is simply the sum of $R_{2,p}$ and $R_{3,p}$, Fig. 8 highlights that R_{high} is not independent of the accretion rate and should not be chosen arbitrarily.

4 CONCLUSIONS & DISCUSSION

We have employed a self-consistent approach to study magnetised and radiatively cooled two-temperature accretion flows around a Kerr black hole in two spatial dimensions. The electrons are subject to radiative processes in the flow, namely Bremsstrahlung, synchrotron, and Comptonization of synchrotron photons. Moreover, we consider Coulomb interaction between electrons and ions, which acts so as to heat the electrons and cool the ions. Finally, we also consider the possibility that the electrons are heated as a result of the turbulent-heating processes. With all these radiative processes taken into account, we have investigated the impact of their inclusion on the accretion flow and how they influence the correlation between the temperatures of the different components. The main results of the present work can be summarised as follows:

(1) The inclusion of the Coulomb interaction and of the radiative cooling impacts the thermodynamical properties of both the ions and electrons. While the turbulent heating is effective only in the funnel and jet-sheath regions, the Coulomb interaction heats the electrons even in the high-density regions of the flow. Because these processes can change the temperature distribution of the electrons significantly, and the latter is closely related to the electromagnetic emission from these accretion flows, our results underline the importance of a two-temperature approach in studying accretion flows around black holes and their imaging.

(2) The accretion rate is a key driver that influences the bulk properties of the flow and the thermodynamics of the electrons and ions. The density of the electrons and ions increases with the accretion rate, which, in turn, increases the radiation-cooling efficiency and the Coulomb-interaction rate. As a result, an increase of the accre-

tion rate leads to electrons that are colder near the black hole but hotter far from it.

(3) We observe qualitatively distinct temperature properties for SANE and MAD accretion modes while maintaining the same accretion rates. In particular, since in the MAD mode the accreted magnetic flux is larger than in the SANE, the amount of synchrotron radiation produced is larger for a given accretion rate. In addition, because the turbulent heating dominates in the funnel and jet-sheath regions, we observe a hotter polar region and a cooler disc region. These differences may become more prominent when the accretion flow is imaged, and they could help distinguishing between MAD and SANE accretion flows via observations. We should note that the comparison between SANE and MAD models is here limited to a single accretion rate; future work will also explore additional MAD models with different accretion rates.

(4) Having to deal with two-temperature fluids clearly requires a different treatment of the temperatures of the electrons, the ions, and of the gas. The temperature ratios T_i/T_e and T_g/T_e show a broad correlation with the plasma- β parameter² and can therefore be expressed in terms of it. The standard $R - \beta$ relation (Mościbrodzka et al. 2016) fits well these correlations, but only for very small or very large values of the plasma- β parameter, i.e., $\beta \lesssim 0.1$ and $\beta \gtrsim 100$. Because outside of these ranges, the $R - \beta$ relation does not provide a good description of the temperature ratios well, we have modified the $R - \beta$ relations by introducing only two additional terms despite having to deal with two-temperature ratios. The new $R - \beta$ relations show a good fit of the correlations between the various temperatures in all the physical scenarios.

(5) The parameters involved in our new $R - \beta$ relations show a clear and strong correlation with the accretion rate. In particular, they are almost constant for very small accretion rates, but drastic variations in size when the accretion rate becomes higher than $\dot{M} \gtrsim 10^{-7} \dot{M}_{\text{Edd}}$. This result, which is in agreement with earlier studies (Dibi et al. 2012; Ryan et al. 2017; Yoon et al. 2020), suggests that a self-consistent magnetised two-temperature accretion flow is necessary to understand accretion flows with large accretion rates.

In summary, our simulation models show that the two-temperature paradigm is important for understanding the thermodynamical properties of electrons and ions in the accretion flow. In particular, it is much more critical if the accretion rate of flow is greater than $\dot{M} \gtrsim 10^{-7} \dot{M}_{\text{Edd}}$. These conditions are those expected to accompany the accretion onto supermassive black holes in low-luminosity active galactic nuclei, where the accretion is expected to be geometrically thick, optically thin, and radiatively inefficient (RIAF) (see Ichimaru 1977; Rees et al. 1982; Reynolds et al. 1996; Narayan et al. 1998; Remillard & McClintock 2006, etc.). Despite the fact that we only considered one black-hole mass for reference in this study, we account for radiative losses in code units, which are normalised by black-hole mass. We also express the accretion rate in terms of the Eddington accretion rate, and therefore the scaling of black-hole mass is taken into account naturally. Hence, our self-consistent two-temperature approach can be used to model the near-horizon emission from supermassive black holes such as Sgr A*, M 87*. Such an application, however, will necessarily require the extension of these simulations to three spatial dimensions so as to guarantee the long-term operation

² In principle, the temperature ratios could also be expressed in terms of the strength of the magnetisation σ . However, since the pressure and rest-mass density are related via an equation of state, the functional form of these alternative relations is expected to be rather similar.

of the MRI and thus avoid the artificial decay of the magnetic field that inevitably accompanies axisymmetric simulations. As a result, we anticipate that the results in the low-magnetised region ($\sigma < 1$) of full 3D GRMHD simulations will be the same as those of our axisymmetric simulations. However, the results from our simulations might not be as realistic as those from 3D GRMHD simulations in the funnel region ($\sigma > 1$) and may be slightly different quantitatively.

Generally, the electron temperature distribution or the distribution of the electron-to-ion temperature ratio (T_e/T_i) also quite similar to the previous studies (e.g., Ressler et al. 2015, 2017; Sądowski et al. 2017; Chael et al. 2018, 2019; Ryan et al. 2018; Dexter et al. 2020a; Mizuno et al. 2021; Yao et al. 2021), apart from certain quantitative differences. Firstly, due to the turbulent heating prescription by Howes (2010, 2011), the electron temperature at the funnel region is very high and the ratio becomes $T_e/T_i > 1$ in the MAD case. Similar results were reported by earlier studies on sub-grid electron heating (e.g., Chael et al. 2019; Event Horizon Telescope Collaboration et al. 2021). Secondly, in the initial condition of our SANE models, we choose a smaller torus in comparison with those considered in earlier simulation work. This fact leaves our SANE models to have accumulated magnetic flux at the event horizon of the order of $\dot{\Phi}/\sqrt{\dot{M}} \sim 1.5$. As a result, the electrons in the funnel region remain colder as compared with other studies (e.g., Sądowski et al. 2017; Dexter et al. 2020a; Yao et al. 2021). Unlike most of the previous works, we do not restrict ourselves to studying the temperatures (T_e, T_i) distributions with different heating prescriptions, but we study the impact of the change in accretion rates by several orders of magnitudes. And further, we go one step forward to compute the correlation of T_e/T_i with the accretion rates. In the future, we plan to do 3D GRMHD simulations at different accretion rates and apply them to the recent observations of M 87*, and Sgr A*.

In the governing Eq. 2, we consider that the radiation flux term is proportional to the radiative cooling rate and the fluid velocity. This approximation is straightforward and computationally efficient to implement to study the impacts of radiation in the accretion flow (e.g., Fragile & Meier 2009; Dibi et al. 2012; Yoon et al. 2020, etc.). However, an M1 closure (Sądowski et al. 2017; Chael et al. 2018, 2019) or a Monte-Carlo scheme (Ryan et al. 2017, 2018; Dexter et al. 2021) are more appropriate treatment for investigating the fluid dynamics coupling with radiation field, although it is much more computationally expensive. We plan to implement such schemes for our future studies. In this study, we chose the Howes (2011) turbulent electron heating model, and for the sake of consistency, we kept it the same for all the simulation models with different physical scenarios considered here. Consideration of different electron heating models (e.g., Rowan et al. 2017; Werner et al. 2018; Kawazura et al. 2019; Zhdankin et al. 2019) may calculate slightly different electron temperatures close to the black hole or the polar region (Chael et al. 2018; Dexter et al. 2020b; Mizuno et al. 2021). However, in the low-magnetised region ($\sigma < 1$), we do not anticipate any major differences in the obtained electron and ion temperatures. Additionally, we fixed the adiabatic index of the electrons to be $\tilde{\Gamma}_e = 4/3$. However, we observed thermally sub-relativistic electrons ($\Theta_e < 1$) in the cooling dominated region of the simulation domain. Electron temperatures calculated in these regions may be slightly over-estimated. We should mention that using variable adiabatic index is more appropriate for studying magnetised accretion flow around black holes (e.g., Sądowski et al. 2017; Dhihingia et al. 2020). We are currently working on such treatment, and we will report the results elsewhere in future.

ACKNOWLEDGEMENTS

This research is supported by the DFG research grant “Jet physics on horizon scales and beyond” (Grant No. FR 4069/2-1), the ERC Advanced Grant “JETSET: Launching, propagation and emission of relativistic jets from binary mergers and across mass scales” (Grant No. 884631), Max Planck partner group grant (MPG-01) at Indian Institute Technology of Indore, the National Natural Science Foundation of China (Grant No. 12273022), and Department of Science and Technology’s Swarnajayanti Fellowship (DST/SJF/PSA-03/2016-17) at IISc Bangalore. The simulations were performed on Pi2.0 and Siyuan Mark-I at Shanghai Jiao Tong University, and Max Planck Gesellschaft (MPG) super-computing resources. LR acknowledges the Walter Greiner Gesellschaft zur Förderung der physikalischen Grundlagenforschung e.V. through the Carl W. Fueck Laureatus Chair. We appreciate the thoroughness and thoughtful comments provided by the reviewers that have improved the manuscript.

DATA AVAILABILITY

The data underlying this article will be shared on reasonable request to the corresponding author.

REFERENCES

- Abramowicz M. A., Czerny B., Lasota J. P., Szuszkiewicz E., 1988, *ApJ*, **332**, 646
- Anantua R., Ressler S., Quataert E., 2020, *MNRAS*, **493**, 1404
- Begelman M. C., Pringle J. E., 2007, *MNRAS*, **375**, 1070
- Chael A., Rowan M., Narayan R., Johnson M., Sironi L., 2018, *MNRAS*, **478**, 5209
- Chael A., Narayan R., Johnson M. D., 2019, *MNRAS*, **486**, 2873
- Chan C.-K., Psaltis D., Özel F., Narayan R., Sadowski A., 2015, *ApJ*, **799**, 1
- Chandrasekhar S., 1939, An introduction to the study of stellar structure
- Colpi M., Maraschi L., Treves A., 1984, *ApJ*, **280**, 319
- Cruz-Orsorio A., et al., 2022, *Nature Astronomy*, **6**, 103
- Davelaar J., Mościbrodzka M., Bronzwaer T., Falcke H., 2018, *A&A*, **612**, A34
- Davelaar J., et al., 2019, *A&A*, **632**, A2
- Del Zanna L., Zanotti O., Bucciantini N., Londrillo P., 2007, *A&A*, **473**, 11
- Dexter J., Agol E., Fragile P. C., 2009, *ApJ*, **703**, L142
- Dexter J., Agol E., Fragile P. C., McKinney J. C., 2010, *ApJ*, **717**, 1092
- Dexter J., et al., 2020a, *MNRAS*, **494**, 4168
- Dexter J., et al., 2020b, *MNRAS*, **497**, 4999
- Dexter J., Scepi N., Begelman M. C., 2021, *ApJ*, **919**, L20
- Dibi S., Drappeau S., Fragile P. C., Markoff S., Dexter J., 2012, *MNRAS*, **426**, 1928
- Dihingia I. K., Das S., Mandal S., 2018, *MNRAS*, **475**, 2164
- Dihingia I. K., Das S., Prabhakar G., Mandal S., 2020, *MNRAS*, **496**, 3043
- Dihingia I. K., Vaidya B., Fendt C., 2021, *MNRAS*, **505**, 3596
- Drappeau S., Dibi S., Dexter J., Markoff S., Fragile P. C., 2013, *MNRAS*, **431**, 2872
- Esin A. A., Narayan R., Ostriker E., Yi I., 1996, *ApJ*, **465**, 312
- Event Horizon Telescope Collaboration et al., 2019, *ApJ*, **875**, L5
- Event Horizon Telescope Collaboration et al., 2021, *ApJ*, **910**, L13
- Event Horizon Telescope Collaboration et al., 2022, *ApJ*, **930**, L16
- Fishbone L. G., Moncrief V., 1976, *ApJ*, **207**, 962
- Fragile P. C., Meier D. L., 2009, *ApJ*, **693**, 771
- Fromm C. M., et al., 2022, *A&A*, **660**, A107
- Gold R., McKinney J. C., Johnson M. D., Doeleman S. S., 2017, *ApJ*, **837**, 180
- Howes G. G., 2010, *MNRAS*, **409**, L104
- Howes G. G., 2011, *ApJ*, **738**, 40
- Ichimaru S., 1977, *ApJ*, **214**, 840
- Igumenshchev I. V., 2008, *ApJ*, **677**, 317
- Kato S., Honma F., Matsumoto R., 1988, *MNRAS*, **231**, 37
- Kawazura Y., Barnes M., Schekochihin A. A., 2019, *Proceedings of the National Academy of Science*, **116**, 771
- Kusunose M., Takahara F., 1988, *PASJ*, **40**, 435
- Kusunose M., Takahara F., 1989, *PASJ*, **41**, 263
- Luo C., Liang E. P., 1994, *MNRAS*, **266**, 386
- Manmoto T., Mineshige S., Kusunose M., 1997, *ApJ*, **489**, 791
- McKinney J. C., Gammie C. F., 2004, *ApJ*, **611**, 977
- Mizuno Y., et al., 2018, *Nature Astronomy*, **2**, 585
- Mizuno Y., Fromm C. M., Younsi Z., Porth O., Olivares H., Rezzolla L., 2021, *MNRAS*, **506**, 741
- Mościbrodzka M., Gammie C. F., Dolence J. C., Shiokawa H., Leung P. K., 2009, *ApJ*, **706**, 497
- Mościbrodzka M., Shiokawa H., Gammie C. F., Dolence J. C., 2012, *ApJ*, **752**, L1
- Mościbrodzka M., Falcke H., Shiokawa H., Gammie C. F., 2014, *A&A*, **570**, A7
- Mościbrodzka M., Falcke H., Shiokawa H., 2016, *A&A*, **586**, A38
- Nakamura K. E., Matsumoto R., Kusunose M., Kato S., 1996, *PASJ*, **48**, 761
- Narayan R., Yi I., 1995, *ApJ*, **452**, 710
- Narayan R., Mahadevan R., Grindlay J. E., Popham R. G., Gammie C., 1998, *ApJ*, **492**, 554
- Narayan R., Sądowski A., Penna R. F., Kulkarni A. K., 2012, *MNRAS*, **426**, 3241
- Nathanail A., Fromm C. M., Porth O., Olivares H., Younsi Z., Mizuno Y., Rezzolla L., 2020, *MNRAS*, **495**, 1549
- Noble S. C., Leung P. K., Gammie C. F., Book L. G., 2007, *Classical and Quantum Gravity*, **24**, S259
- Olivares H., Porth O., Davelaar J., Most E. R., Fromm C. M., Mizuno Y., Younsi Z., Rezzolla L., 2019, *A&A*, **629**, A61
- Piran T., 1978, *ApJ*, **221**, 652
- Porth O., Olivares H., Mizuno Y., Younsi Z., Rezzolla L., Mościbrodzka M., Falcke H., Kramer M., 2017, *Computational Astrophysics and Cosmology*, **4**, 1
- Porth O., et al., 2019, *ApJS*, **243**, 26
- Porth O., Mizuno Y., Younsi Z., Fromm C. M., 2021, *MNRAS*, **502**, 2023
- Pringle J. E., 1976, *MNRAS*, **177**, 65
- Rajesh S. R., Mukhopadhyay B., 2010, *MNRAS*, **402**, 961
- Rees M. J., Begelman M. C., Blandford R. D., Phinney E. S., 1982, *Nature*, **295**, 17
- Remillard R. A., McClintock J. E., 2006, *ARA&A*, **44**, 49
- Ressler S. M., Tchekhovskoy A., Quataert E., Chandra M., Gammie C. F., 2015, *MNRAS*, **454**, 1848
- Ressler S. M., Tchekhovskoy A., Quataert E., Gammie C. F., 2017, *MNRAS*, **467**, 3604
- Reynolds C. S., Di Matteo T., Fabian A. C., Hwang U., Canizares C. R., 1996, *MNRAS*, **283**, L111
- Rezzolla L., Zanotti O., 2013, Relativistic Hydrodynamics
- Rowan M. E., Sironi L., Narayan R., 2017, *ApJ*, **850**, 29
- Ryan B. R., Ressler S. M., Dolence J. C., Tchekhovskoy A., Gammie C., Quataert E., 2017, *ApJ*, **844**, L24
- Ryan B. R., Ressler S. M., Dolence J. C., Gammie C., Quataert E., 2018, *ApJ*, **864**, 126
- Sano T., Inutsuka S.-i., Turner N. J., Stone J. M., 2004, *ApJ*, **605**, 321
- Sarkar S., Chattopadhyay I., Laurent P., 2020, *A&A*, **642**, A209
- Shakura N. I., Sunyaev R. A., 1973, *A&A*, **500**, 33
- Shapiro S. L., Lightman A. P., Eardley D. M., 1976, *ApJ*, **204**, 187
- Shcherbakov R. V., Penna R. F., McKinney J. C., 2012, *ApJ*, **755**, 133
- Shiokawa H., Dolence J. C., Gammie C. F., Noble S. C., 2012, *ApJ*, **744**, 187
- Sądowski A., Wielgus M., Narayan R., Abarca D., McKinney J. C., Chael A., 2017, *MNRAS*, **466**, 705
- Spitzer L., 1965, Physics of fully ionized gases
- Sygne J. L., 1957, The Relativistic Gas.. North-Holland Pub. Co.; Interscience Publishers
- Tchekhovskoy A., Narayan R., McKinney J. C., 2011, *MNRAS*, **418**, L79
- Wandel A., Liang E. P., 1991, *ApJ*, **380**, 84

- Werner G. R., Uzdensky D. A., Begelman M. C., Cerutti B., Nalewajko K., 2018, *MNRAS*, 473, 4840
- White T. R., Lightman A. P., 1989, *ApJ*, 340, 1024
- Yao P. Z., Dexter J., Chen A. Y., Ryan B. R., Wong G. N., 2021, *MNRAS*, 507, 4864
- Yoon D., Chatterjee K., Markoff S. B., van Eijnatten D., Younsi Z., Liska M., Tchekhovskoy A., 2020, *MNRAS*, 499, 3178
- Zhdankin V., Uzdensky D. A., Werner G. R., Begelman M. C., 2019, *Phys. Rev. Lett.*, 122, 055101

APPENDIX A: CORRELATION OF BEST-FIT PARAMETERS \dot{M}

The values of the best-fit parameters for the temperature ratio T_i/T_e ($R_{1-3,p}, \beta_{\text{br}}$) for different simulation models are shown in Table 2. To explore their correlations with the accretion rate, we find the best-fit of these parameters with the same. The explicit expressions of these parameters in terms of the accretion rate are given below,

$$\begin{aligned}
 R_{1,p}(\dot{M}/\dot{M}_{\text{Edd}}) &= R_{10} + R_{11}(\dot{M}/\dot{M}_{\text{Edd}})^{0.54}, \\
 R_{2,p}(\dot{M}/\dot{M}_{\text{Edd}}) &= R_{20} + R_{21}(\dot{M}/\dot{M}_{\text{Edd}})^{0.68}, \\
 R_{3,p}(\dot{M}/\dot{M}_{\text{Edd}}) &= R_{30} + R_{31}(\dot{M}/\dot{M}_{\text{Edd}})^{0.41}, \\
 \beta_{\text{br}}(\dot{M}/\dot{M}_{\text{Edd}}) &= \beta_{\text{br}0} + \beta_{\text{br}1}(\dot{M}/\dot{M}_{\text{Edd}})^{0.16}.
 \end{aligned}
 \tag{A1}$$

Here, the values of the different constants are given by $R_{10} = 2.81$, $R_{11} = -1.22 \times 10^2$, $R_{20} = 1.60$, $R_{21} = 4.14 \times 10^3$, $R_{30} = 9.12$, $R_{31} = -6.68 \times 10^2$, $\beta_{\text{br}0} = 62.4$, $\beta_{\text{br}1} = -2.50 \times 10^2$. In Fig. 8, we show the plot of these functions with dashed lines along with values of $(R_{1-3,p}, \beta_{\text{br}})$ for different simulation models. The figure essentially shows that the best-fit parameters correlate thoroughly with the mass-accretion rate. Note that expressions (A1) have been derived from SANE models only. Because the cooling and heating processes – which are obviously the same for SANE and MAD accretion modes – depend on the strength of the magnetic field, it is natural to expect that while the functional form will be the same, small changes in the values of the coefficients $R_{1,k}$, $R_{2,k}$, $R_{3,k}$, and β_{br} will appear when evaluating expressions (A1) for MAD accretion modes.

This paper has been typeset from a $\text{\TeX}/\text{\LaTeX}$ file prepared by the author.